ADVANCED OPTICAL MATERIALS
www.advopticalmat.de

Anharmonic Exciton-Phonon Coupling in Metal-Organic Chalcogenides Hybrid Quantum Wells

Christoph Kastl, Pietro Bonfà, and Lorenzo Maserati**

In contrast to inorganic quantum wells, hybrid quantum wells (HQWs) based on metal-organic semiconductors are characterized by relatively soft lattices, in which excitonic states can strongly couple to lattice phonons. Therefore, understanding the lattice's impact on exciton dynamics is essential for harnessing the optoelectronic potential of HQWs. Beyond 2D metal halide perovskites, layered metal-organic chalcogenides (MOCs), which are an air-stable, underexplored material class hosting room-temperature excitons, can be exploited as photodetectors, light emitting devices, and ultrafast photoswitches. Here, the role of phonons in the optical transitions of the prototypical MOC $[AgSePh]_\infty$ is elucidated. Impulsive stimulated Raman scattering (ISRS) allows the detection of coherent exciton oscillations driven by Fröhlich interaction with low-energy optical phonons. Steady state absorption and Raman spectroscopies reveal a strong exciton-phonon coupling (Huang-Rhys parameter ≈1.7) and its anharmonicity, manifested as a nontrivial temperature-dependent Stokes shift. The ab initio calculations support these observations, hinting at an anharmonic behavior of the low-energy phonons <200 cm^{-1}. These results untangle complex exciton-phonon interactions in MOCs, establishing an ideal testbed for room-temperature many-body phenomena.

1. Introduction

Metal organic chalcogenides (MOCs) and 2D metal halide perovskites (MHPs) are examples of hybrid quantum wells (HQWs) hosting tightly bound 2D excitons. In both material classes, the excitonic resonances are stable at room temperature and could be exploited for a wide class of optoelectronic applications, such as LEDs, photodetectors, and ultrafast photoswitches.[1,2] Yet in contrast to hybrid perovskites, MOCs are also stable under working conditions, and recent improvements in their synthesis approaches allow producing high-quality samples suitable both for spectroscopic investigation and device fabrication.[3–5] In particular, the excitonic behavior of $[AgSePh]_\infty$, a prototypical MOC, has just been investigated by us,[6,7] and two other groups,[8–10] highlighting strongly bound anisotropic resonances with blue, direct gap emission and very short lifetime. This short exciton lifetime is peculiar and could be potentially leveraged for ultrafast optical applications. As we recently reported, the $[AgSePh]_\infty$ ultrafast de-excitation appears to be dominated potentially by intrinsic self-trapping of excitons.[6,7] Such self-trapping of carriers often occurs in semiconductors with a large electron–phonon coupling.[11] In the latter case, a proper description of optical excitations needs to consider the dressing of excitons with lattice phonons, which ultimately gives rise to a new quasi-particle, the exciton-polaron, in the strong interaction limit. While the subfield of 2D MHPs already reported several experiments highlighting the important role of phonons and lattice distortions in the optical transitions and carrier dynamics,[12–17] the HQWs based on MOCs still lack an understanding of such interplay between excitons and phonons.

Here, we study exciton-phonon coupling in the prototypical MOC $[AgSePh]_\infty$ by a combination of time-resolved and time-integrated optical spectroscopies. Impulsive stimulated Raman scattering (ISRS)[18,19] via resonant transient absorption

C. Kastl, L. Maserati
The Molecular Foundry
Lawrence Berkeley National Laboratory
Berkeley California 94720, USA
E-mail: christoph.kastl@wsi.tum.de; lorenzo.maserati@unibo.it
C. Kastl
Walter Schottky Institute and Physik Department
Technical University of Munich
85748 Garching, Germany
The ORCID identification number(s) for the author(s) of this article can be found under https://doi.org/10.1002/adom.202202213.

DOI: 10.1002/adom.202202213

P. Bonfà
Dipartimento di Scienze Matematiche, Fisiche e Informatiche
Universitá di Parma
Parma 43124, Italy
P. Bonfà
Centro S3
CNR-Istituto Nanoscienze
via Campi 213/A, Modena I-41125, Italy
L. Maserati
Center for Nano Science and Technology @PoliMi
Istituto Italiano di Tecnologia
Milan 20133, Italy
L. Maserati
Dipartimento di Fisica e Astronomia
Università di Bologna
Viale Berti-Pichat 6/2, Bologna 40127, Italy

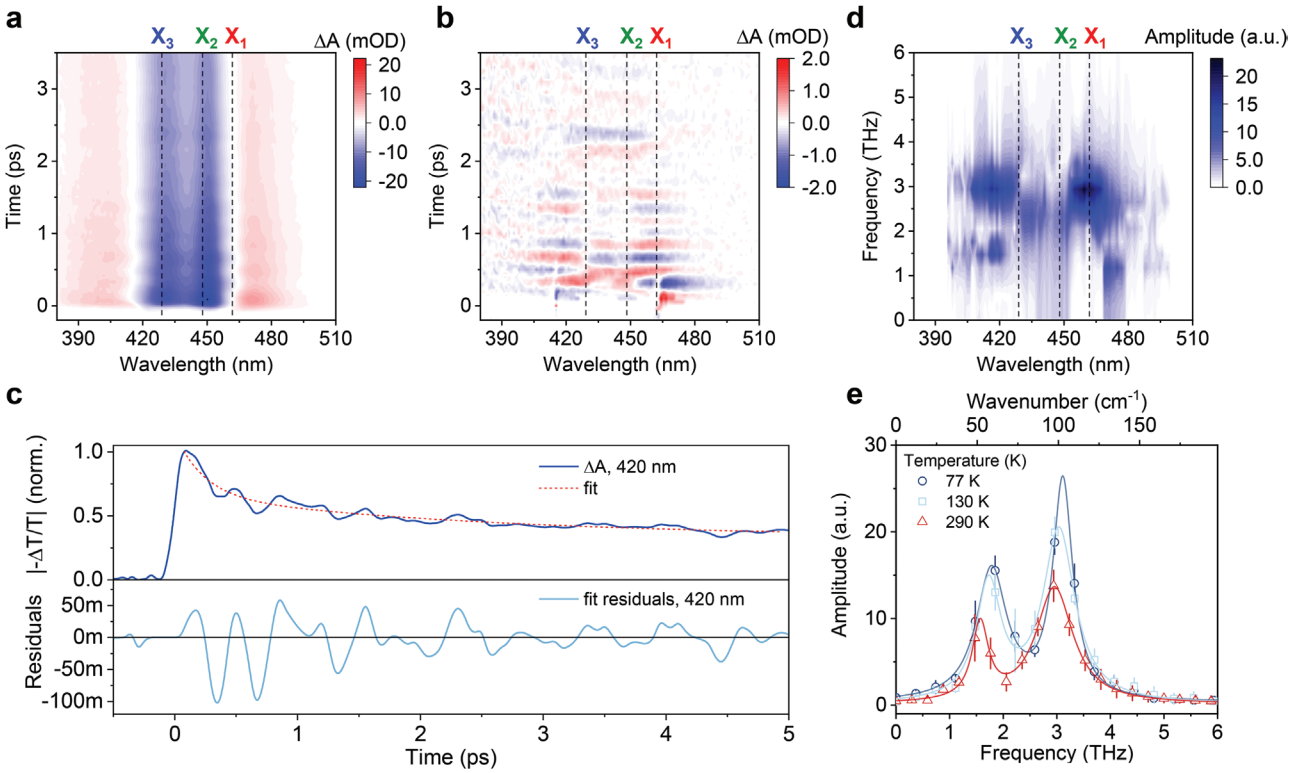

Figure 1. Resonant impulsive stimulated Raman scattering (resonant ISRS) of $[AgSePh]_\infty$ revealed by transient absorption (TA). a) Room temperature, broadband TA near the main exciton transitions: 464 nm (2.672 eV) X_1, 453 nm (2.738 eV) X_2, and 432 nm (2.870 eV) X_3. b) After subtraction of the decay dynamics, the TA reveals coherent oscillations. c) Example of the procedure used to extract the coherent oscillations from the TA data. The transient absorption map in (a) is cut at a fixed wavelength (here 420 nm, blue line), fitted by a sum of exponentials and (dashed red line) and the fit residuals are extracted (light blue line). d) Fast Fourier transform (FFT) of (b). Two main oscillation peaks appear throughout the probe energy spectrum. e) Integrated FFT signals around X_3 (≈425 nm), plotted versus frequency (or phonon energy) at different temperatures. With decreasing temperature, the oscillation frequencies shift to higher values.

reveals coherent coupling of the excitonic transitions to distinct phonons at 56 cm^{-1} and 98 cm^{-1}, while temperature-dependent absorption and photoluminescence (PL) spectroscopies both suggest a further coupling to phonons with an average energy in the range of 150 ± 19 cm^{-1} to 175 ± 10 cm^{-1}, and they put the average coupling strength, i.e., the Huang–Rhys factor,[20] in the intermediate-to-strong regime. Non-resonant steady-state Raman spectra show matching, low-energy optical phonon modes (56 cm^{-1}, 98 cm^{-1}, and 195 cm^{-1}) associated with the inorganic quantum well planes, where the excitonic wavefunctions are mainly localized,[6] as well as a multitude of high energy phonons (>200 cm^{-1}) modes associated mostly with specific molecular modes of the organic ligands separating the quantum wells. We find several indications of anharmonicity in the spectroscopic analysis. First, ab initio simulations based on density functional theory (DFT) and carried out in the harmonic approximation, reproduce the high-energy Raman active modes above 200 cm^{-1}, but fail to reproduce the experimentally observed low-energy Raman modes below 200 cm^{-1}. Second, starting at around 220 K, we simultaneously find an unusual activation of phonon intensities, a departure of the temperature-dependent Stokes shift from typical semiconductor models, as well as an emerging Rayleigh peak in the Raman spectrum below 200 cm^{-1}, which we interpret as signatures of phonon anharmonicity. Finally, we detected a strong in-plane anisotropy of the 98 cm^{-1} phonon that aligns with the already reported in-plane anisotropy of one of the excitons.[6,7] Overall our results highlight the general importance of exciton coupling to optical phonons in this class of materials and they further suggest that also the peculiar spatial symmetry of the excitonic states and phonon modes needs to be accounted for in a proper treatment of exciton–phonon coupling.[21]

2. Results and Discussion

The broadband transient absorption (TA) measurement in **Figure 1**a shows the evolution of the free carrier and exciton population around the lowest-lying exciton transitions after pumping at 430 nm (2.883 eV). At room temperature, the main excitonic transitions occur at 464 nm (2.672 eV) X_1, 453 nm (2.738 eV) X_2, and 432 nm (2.870 eV) X_3. As we recently reported, the TA signal is dominated by ground state bleaching and bandgap renormalization on the picosecond timescale, induced by free-carrier and exciton screening.[7] As apparent most prominently near the zero-crossings of the TA signal $\Delta A(t)$, the decay dynamics are superimposed by a sub-picosecond oscillation. The oscillation dynamics (Figure 1b) can be extracted by a fitting procedure, where we subtracted the decay components for each probe wavelength revealing a clear oscillation pattern with a period on the order of a few hundred femtoseconds for all

excitonic transitions (Figure 1c and SI for details). Because the three excitonic states are each separated by >50 meV, we can immediately rule out coherent quantum beating as the origin of the observed oscillations. In the latter case, the expected period would be below 100 fs. Instead, the oscillations can be understood as the result of resonant impulsive stimulated Raman scattering (resonant ISRS).[22,23] The oscillation frequency represents the energy of impulsively generated optical phonons that couple to the optical transitions. These excited phonons transiently modulate the excitonic absorption (and therefore the dielectric function of the material) over time.[24,25] In particular, the oscillations indicate a displacement of the excited-state potential energy surface along the normal modes that appear in ΔA(t). We find that the amplitude modulation $\Delta A(t)$ is proportional to $\partial\varepsilon_2/\partial E$ where ε_2 is the imaginary part of the dielectric constant and E is the absorption energy (Figure S1, Supporting Information), as is expected in the case of ISRS excited close to real electronic transitions.[26,27] In agreement with this picture, the oscillation amplitude scales linearly with the pump fluence (Figure S2, Supporting Information),[22] the oscillation is antisymmetric around the energy positions of the exciton ground states (Figure S3, Supporting Information), and the process displays resonant character (Figure S4, Supporting Information). All the above observations allow us also to exclude interference effects as signal sources.[27,28] On the other hand, the assignment of a particular exciton as a major player in the phonon coupling is not trivial at this stage, as the prominent TA signal is related to the ground state bleaching and this is common to the three observed excitons. In other words, the oscillations can be caused by just one exciton, while the other two excitonic transitions are impacted by it.

From the Fourier transform of the oscillation pattern (Figure 1c), two main frequencies centered approximately at 1.75 THz and 3 THz can be identified. The corresponding energy scales are 56 cm^{-1} (7 meV) and 98 cm^{-1} (12 meV). By performing resonant ISRS experiments over temperature, we find that in both cases the oscillation frequency increases with decreasing lattice temperature (Figure 1d, Figures S5 and S6, Supporting Information), due to a stiffening of the lattice at low temperature.[28] The Lorentzian linewidth of the phonon mode at 12 meV increases with increasing temperature indicating a shortening of the phonon coherence time. The latter can be attributed to the presence of anharmonic terms in the vibrational potential energy,[29] and as a consequence, it is conceivable that the 12 meV mode can undergo inelastic phonon–phonon scattering relaxing into two counter-propagating longitudinal acoustic (LA) phonons via the so-called Klemens decay.[30] This characteristic distinguishes the 12 meV phonon from the 7 meV phonon, whose temperature-dependent homogeneous linewidth follows a different trend (Figures S5 and S6, Supporting Information), suggesting a diverse nature of the two.

Due to the relatively large energies of the two detected phonons, we focus our discussion on optical phonons. Considering the high electronegativity difference of 0.7 eV between the inorganic constituents Ag and Se, when compared for example to 0.4 eV for GaAs, and the resulting strong polarity of the inorganic layer bonds, we can anticipate the long-range polar (Fröhlich) interaction[12] to be the dominant exciton scattering process. Indeed, we find that the Raman scattering of $[AgSePh]_\infty$ is preferentially co-polarized (Figure S7, Supporting Information), favoring the hypothesis of Fröhlich interaction over deformation potential.[31,32]

To estimate the strength of exciton-phonon coupling from basic material properties, we follow the approach described in refs. [33,36] and we consider the electron-phonon and hole-phonon interaction separately, since a complete treatment for the exciton-polaron in the weak localization limit (Wannier exciton) needs further extensions of the existing polaron theories.[37,38] Based on these assumptions, the Fröhlich coupling constant for electrons (holes) can be calculated according to Equation (1):

$$\alpha_{e-ph} = \frac{e^2}{\hbar}\frac{1}{4\pi\varepsilon_0}\left(\frac{1}{\varepsilon_\infty}-\frac{1}{\varepsilon_s}\right)\sqrt{\frac{m^*}{2\hbar\omega}} \tag{1}$$

Here e is the charge of the carrier, ħ is the reduced Planck's constant, ε_0 is the vacuum dielectric constant, ε_∞ and ε_S are the optical and static dielectric constants, respectively, m^* is the effective electron (hole) mass and $\hbar\omega$ is the phonon energy. Except for the phonon energies, all parameters were derived from DFT (see Supporting Information for details). For the phonon modes at 12 meV and 7 meV, α_{e-ph} results to be 1.83 (2.43 for holes) and 2.45 (3.26 for holes), respectively (see Table S1, Supporting Information, for parameters values), positioning the exciton-coupling strength for both phonons at the edge of the weak-intermediate regime ($\alpha_{e-ph} = 1-3$), leading to a formation of intermediate-large exciton-polarons.[34,37,39]

To experimentally assess the exciton-phonon coupling strength, we turn our attention to the linear absorption and photoluminescence spectra over temperature (**Figure 2**a,b). To separate the absorption peak position of the lowest-energy exciton X_1 from the overlapping X_2 and X_3 resonances, we analyze the second derivative of the absorption (Supporting Figure S8). Furthermore, we extend the dataset down to 5 K by incorporating TA data from ref. [7]. For the PL emitted through X_1, we consider Voigt line shapes (Figure S8, Supporting Information). The X_1 peak energy versus temperature is shown in Figure 2c for both absorption and photoluminescence.

Both curves display a characteristic red-shift with rising temperature, which can be well described over the entire temperature range with the O'Donnell-Chen model:[40]

$$E_g(T) = E_{g0} - S\cdot\hbar\omega\left[\coth\left(\hbar\omega/2k_BT\right)-1\right] \tag{2}$$

The latter is a commonly used, semi-empirical model to describe the temperature dependence of the (optical) bandgap in semiconductors due to electron-phonon coupling. In this model, E_{g0} is the energy gap at 0 K, k_B is the Boltzmann constant, ħ is the reduced Plank constant, T is the temperature, S, the Huang-Rhys parameter, is a dimensionless coupling constant, and ω is an average phonon frequency involved in the optical transition.[40] The fitting parameters are reported in **Table 1**. We find approximately a value of 1.7 for the coupling constant and ≈22 meV for the phonon energy. The value of the coupling constant compared to similar systems confirms the intermediate-strong exciton-phonon coupling regime derived from the theoretical expectations above.[27]

The same model applied to the PL energy shift yields comparable parameters. However, upon closer inspection, the PL fitting does not capture the last data points near room temperature

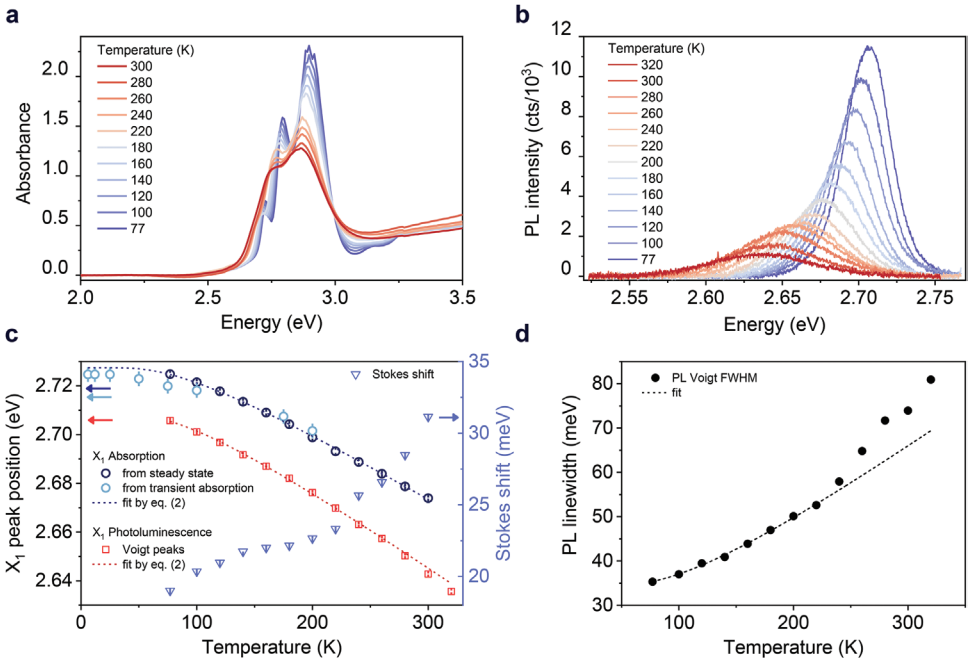

Figure 2. Impact of phonon coupling on absorption and photoluminescence. a) Steady state absorption and b) photoluminescence from room temperature to 77 K. The lowest lying exciton (X_1) is analyzed in panels (c) and (d). c) Both the absorption (open circles) and emission (open squares) energy of X_1 red-shifts as temperature increases. The temperature trend can be fitted (dashed lines) with Equation (2). The Stokes shift (open triangles) indicates the difference between absorption and emission. d) Photoluminescence linewidth of X_1. The dashed line is a fit considering both acoustic and Fröhlich exciton-phonon interaction (see Supporting Information).

(red curve in Figure 2c). In fact, by deriving the value for the Stokes-shift – the difference in the absorption versus photoluminescence peak (blue data points in Figure 2c) – it is clear that the PL energy experiences a suddenly enhanced red-shift above 220 K. This temperature dependence does not fit in the classical Frank-Condon framework where the coupling constant is assumed to be temperature-independent and the temperature dependence arises solely from the occupation of the phonon modes. The observed Stokes-shift in $[AgSePh]_\infty$ does neither follow the trend reported for inorganic quantum wells,[41,42] nor quantum dots.[43] Instead, it shares some similarities with liquid-like dielectric solvation that have been recently discussed for band edge carriers in metal halide perovskites.[28] Indeed, our findings suggest that, similar to the 2D MHPs case,[28] in MOCs, the carrier-lattice coupling strength, namely the effective Fröhlich coupling constant, is *T*-dependent, at least above a certain temperature threshold of ≈220 K.

A similar onset behavior can be found in the PL linewidth (Figure 2d). The dashed line denotes a fit with a standard model introduced for inorganic semiconducting quantum wells (for details see Supporting Information, PL fitting discussion),[44,45] for the description of excitonic semiconductors with acoustic and Fröhlich exciton-phonon interaction, and recently applied to metal halide perovskites.[46,47] A clear deviation from this model can be seen for high temperatures starting approximately at 220 K. From the PL linewidth analysis (cf. absorption analog, Figure S9, Supporting Information) we can further estimate the exciton-phonon coupling γ_{LO} (≈50 meV) confirming again an intermediate-strong coupling and falling in the reported range for 2D MHPs (40–60 meV).[46]

To complete the picture of the phonons involved in the optical transition, we turn to nonresonant, steady-state Raman scattering. **Figure 3**a displays the temperature-dependent Raman spectra of a nanocrystalline (NC) $[AgSePh]_\infty$ film. In previously reported Raman spectra at room temperature,[4] the broad peak at low wavenumbers was subtracted as an experiment-related baseline. Yet, as the temperature-dependent data demonstrates, this background is suppressed at low temperatures, and, therefore, it has to be interpreted as a boson peak or a Rayleigh wing. The Boson peak has been reported for glassy materials, it is related to the accumulation of disorder in noncrystalline solids, and it typically displays a peak shape.[48,49]

Instead, the Rayleigh wing is observed in Raman experiments on liquids or solids close to the melting transition.[50,51] It has been also observed in 2D MHPs, likely caused by the motion of organic perovskite cations subject to dynamic anharmonic disorder,[52,53] or by mixing of zone-folded longitudinal acoustic phonons corresponding to the periodicity of the layered superlattice structure.[54] Considering the shape of the signal, the structure of our material, and its behavior in terms of temperature-dependent dielectric constant, we put forward the Rayleigh wing as the correct interpretation of the high background Raman signal shown in Figure 3a.

Table 1. Fitted parameters from Equation (2) applied to X_1 energy for absorption and PL.

X_1	E_{g0} [meV]	S	$\hbar\omega$ [meV]
Absorption	2,727 ± 0.6	1.64 ± 0.03	21.8 ± 1.2
Photoluminescence	2,710 ± 1	1.77 ± 0.08	18.6 ± 2.3

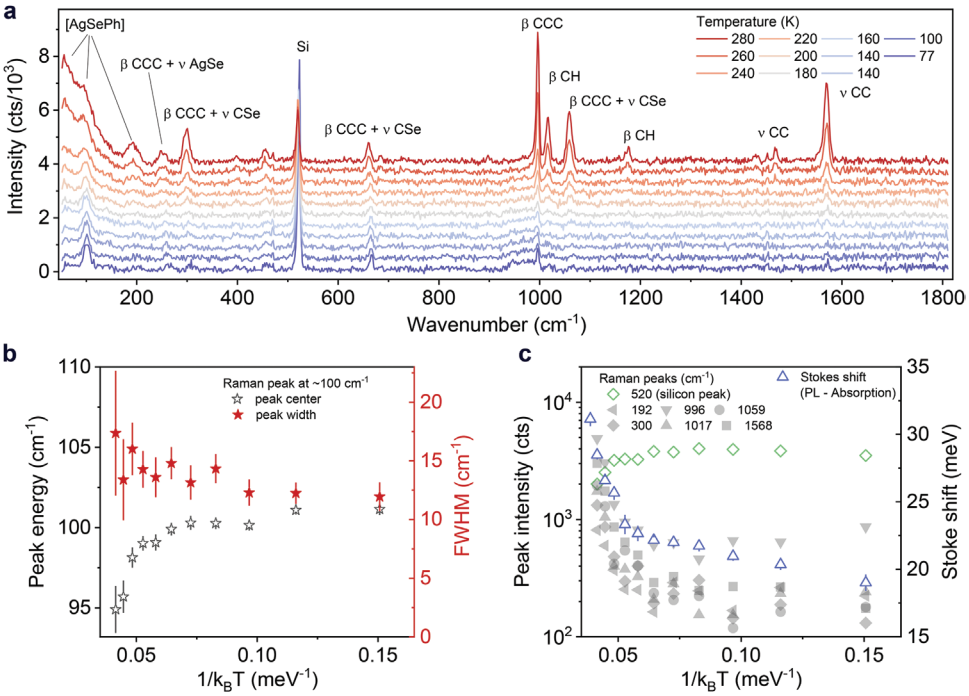

Figure 3. Raman scattering of $[AgSePh]_\infty$. a) Temperature-dependent, non-resonant Raman spectra of a nanocrystalline (NC) film (532 nm excitation). The main peaks are labeled according to ref. [4]. The low-frequency peaks (56, 98, 195 cm^{-1}) are assigned to intrinsic $[AgSePh]_\infty$ modes linked to the inorganic planes. b) The Raman mode near 98 cm^{-1} experiences a blue-shift as temperature decreases (due to lattice stiffening) and a decrease in FWHM (due to reduced inhomogeneous broadening). c) Intensity variation of the main Raman peaks over inverse temperature (gray symbols) showing a thermally activated process with an energy of ≈0.2 eV. The Stokes-shift between PL and absorption energy (blue triangles) reveals a similar trend. The concurrently measured silicon Raman at 520 cm^{-1} (open diamonds) is shown for comparison.

Consistent with Figure 1, we observe Raman peaks at 56 cm^{-1} (7 meV) and 98 cm^{-1} (12 meV), which coincide exactly with the coherent oscillations of the TA signal. Due to the thermal background and the detection limit of our setup, the phonon at 56 cm^{-1} is identified, but not clearly resolved over different temperatures. For the phonon mode at 98 cm^{-1} (Figure 3b), we find a blue-shift as the temperature is lowered (stiffening) as well as a decrease of the FWHM (decreased phonon-phonon scattering), in line with the resonant ISRS experiment (cf. Figure 1d). Generally, all phonon modes below 320 cm^{-1} experience stiffening, suggesting these resonances are linked to the inorganic plane's motion in opposition to the high energy Stokes peaks, whose energies do not vary with temperature (Figure S10, Supporting Information). Since the excitons are largely confined within the inorganic layers, we can restrict the subset of phonons involved mainly in the PL process to the ones with energy <320 cm^{-1} (40 meV). In particular, the third intrinsic broad $[AgSePh]_\infty$ phonon ~195 cm^{-1} (24 meV) approximately corresponds to the absorption/PL phonon energy fit from Equation (2) (cf. Figure 3a), suggesting its involvement in the exciton scattering process that was not detectable by ISRS. This may be due to an enhanced scattering probability and, therefore, shortened coherence time of this phonon mode, below the temporal resolution of our TA setup.

Finally, the peaks at 56 cm^{-1} and 98 cm^{-1} show different relative behavior over the temperature in terms of frequency shift and FWHM (as already revealed by resonant ISRS). Non-resonant Raman further highlights a difference in their intensities trend: while the phonon at 56 cm^{-1} slightly increases with temperature, the phonon at 98 cm^{-1} tends to decreases with temperature (cf. Figure 3a, Figure S11, Supporting Information). Interestingly, all other Raman peaks, which are linked to vibrations/rotations/stretching of the organic ligands,[4] and the Rayleigh wing, exhibit a very different, activated behavior with a steep growth of intensity beyond a certain temperature threshold (Figure 3c, Figure S12, Supporting Information). For reference, the silicon peak intensity (at 520 cm^{-1}) follows a well-studied, opposite trend.[53–55] To the best of our knowledge, such unusual behavior has not been reported in the literature and demands further investigation. Phenomenologically, both the intensities of the Raman peaks and the Stokes shift from Figure 2c scale with a temperature-dependent Arrhenius behavior with an activation energy of ≈0.2 eV (Figure S12, Supporting Information). This correlation suggests that the activation of Raman modes may be the origin of the sudden PL FWHM broadening above that temperature. From this observation, we suggest that above 220 K, the crystalline order might undergo a subtle phase change, where the phenyl groups are likely free to move, giving rise to the activated behavior of their Raman intensity and the steep increase of the Rayleigh wing. This speculation is supported by the fact that two distinct stable phases are reported for $[AgSePh]_\infty$,[5,6,56] and it is plausible that they coexist in different domains as hinted by the transmission electron microscopy (TEM) diffraction experiments reported in ref. [6].

To take a step further into the description of the electronic and vibrational properties of the material, we run ab initio

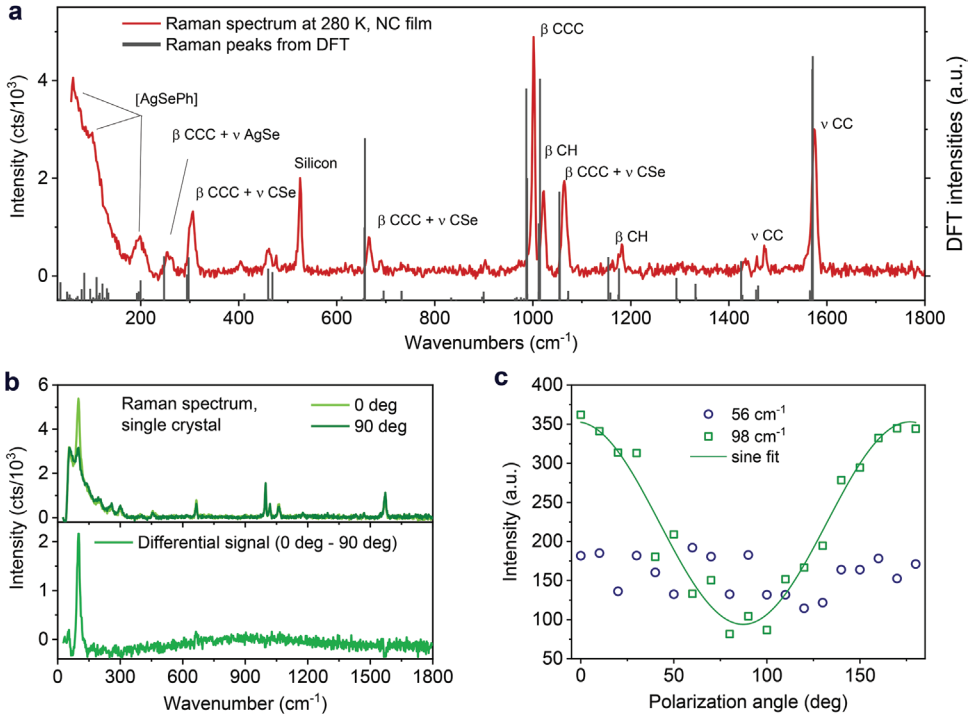

Figure 4. In-plane anisotropic phonons in $[AgSePh]_\infty$. a) Room temperature Raman spectra for $[AgSePh]_\infty$ and nanocrystalline film at 280 K compared to the DFT calculated Raman modes for a randomly oriented NC sample (dark gray bars). b) Room temperature linearly polarized Raman spectra for $[AgSePh]_\infty$ single crystal acquired at 0 (light green) and 90 degrees (green), corresponding to the excitation beam electrical field parallel to the [100] and [010] crystal directions, respectively. The laser and the detector are copolarized. c) Angle resolved peak intensity for the low energy phonons 56 cm^{-1} (blue dots) and 98 cm^{-1} (green squares), fitted with a sinusoidal function.

simulations based on DFT, on the relaxed $[AgSePh]_\infty$ structure (see Experimental Section, discussion in the Supporting Information and Figure S13 there). The vibrational properties have been obtained for the Γ point with density functional perturbation theory (DFPT). We note that the comparison between experimental and theoretical Raman intensities should be taken with some care. First, the NC film is not strictly randomly oriented due to a slight preferential orientation of the NC layer in contact with the substrate. Second, the ab initio estimate of the Raman scattering activity only includes the local part of the density functional without the gradient correction. Having said that, the relative Raman scattering intensities of the calculated phonon modes align to a large extent with the experimentally observed peaks (**Figure 4**a). Notably though, the low energy part of the spectrum (<200 cm^{-1}) does not show two prominent peaks as experimentally observed, but two groups made of many nearly degenerate modes. This theoretical observation suggests that the strong 56 cm^{-1} and 98 cm^{-1} peaks arise from phonon mixing, an effect that by construction cannot be captured by our calculations. As stated in other terms, the mismatch between theory and experiments may be caused by a substantial anharmonic behavior in the low-energy optical phonons. Moreover, we speculate that a breakdown of the harmonic framework can also be the cause of the experimentally observed rising of the Rayleigh wing at higher temperatures.

Finally, we considered a $[AgSePh]_\infty$ single crystal, where due to the anisotropic structure, the polarization of the excitonic resonances was shown to display a highly anisotropic character as well, with the X_2 (X_1 and X_3) resonance being polarized along the [100] direction ([010] direction).[6] Similarly, the crystalline anisotropy can be reflected in the Raman modes, and therefore in the exciton-phonon coupling. We thus resolve the polarization-dependent Raman intensity with respect to the crystal orientation. Figure 4b shows the Raman spectra recorded when the incident beam has the electrical field polarized along the [100] crystal direction (0°) and along the [010] crystal direction (90°). While most of the spectrum is insensitive to the polarization direction, the phonon at 98 cm^{-1} shows a distinct anisotropy (Figure 4c) with a modulation depth of ≈63%. The maximum intensity is reached for polarization parallel to the [100] crystal direction, where also the X_2 exciton shows its intensity maximum.[6] In light of this observation, we speculate that the strongest coherent exciton-phonon coupling actually involves the middle exciton X_2, as also suggested by the fact that the maximum oscillation intensity for detuned pumping in transient absorption experiments (Figure S4, Supporting Information) was achieved for resonantly pumping X_2 at 447 nm.

Lastly, we comment on the role of lattice phonons in the self-trapped exciton (STE) formation, we recently reported.[7] While the exciton self-trapping takes up to 10 ps at room temperature,[7] with a time scale typically associated with acoustic phonon generation,[36] we did not find experimental evidence of the involvement of acoustic phonons in the exciton scattering process, which may possibly be due to instrumental limitations. On the other hand, the coherent exciton coupling with optical phonons is unambiguous and considering their dephasing time (≈1–2 ps)

one could correlate this time scale with the STE initial formation, advancing the idea of the optical phonons' involvement in the exciton localization process.

3. Conclusions

Depending on the interactive nature and range, the electron–lattice coupling or polaronic effect can arise from the long-range electrostatic polarization response (Fröhlich interaction) and short-range deformation potential (Holstein interaction).[38] The former dominated in ionic materials, while the latter is more relevant in "soft" materials featuring dynamic lattice distortion and anharmonic phonons. Similarly, for what is being reported on 2D MHPs,[57] we showed multiple evidence suggesting $[AgSePh]_\infty$ to be an edge case where the two scenarios overlap. At the moment it is still unclear if the $[AgSePh]_\infty$ excitons are pure eigenstates of the Hamiltonian or whether a polaron picture, in which phonons are "dressing" the electrons and holes, is more adequate to describe the optical transitions. To tip in favor of the latter hypothesis we observe that based on their energy spacing, the optical resonances cannot be phonon-replica (it would require a constant spacing of 10 – 20 meV) nor higher energy excitonic states (they would be spaced proportionally to n^{-2}, where n are the hydrogen-like energy levels).[58] They must therefore be distinct entities. Nevertheless, the multiple excitons and phonons involved in the optical transitions depict a complex scenario, where definitive answers regarding their interaction are yet to be obtained.

On the way to unearth the convoluted many-body interaction in HQWs, we reported $[AgSePh]_\infty$ transient absorption dynamics at picosecond time-scales displaying pronounced oscillations with two distinct frequencies corresponding to the 7 meV (56 cm^{-1}) and 12 meV (98 cm^{-1}) optical phonon modes. The linear absorption and photoluminescence peak energy and linewidth analysis by the Chen-O'Donnell model suggested an average phonon energy of about 22 meV to dominate the steady-state optical transitions. Therefore, phonons at 7 meV and 12 meV could be involved in a multiple scattering process. Alternatively, considering the non-resonant Raman spectrum,[4] the third (and last) characteristic $[AgSePh]_\infty$ phonon at ≈24 meV (195 cm^{-1}) could be the one dominating the absorption/PL process. Furthermore, we found a peculiar temperature-activated behavior of the Raman Stokes modes, in particular of the high energy phonon modes associated with the organic ligands. This activation coincides with a nonlinear temperature dependence of the PL Stokes shift, indicating a possible anharmonic behavior of the lattice phonons that couple to excitonic transitions. This behavior is reminiscent of a liquid-like dielectric solvation and it points towards a thermal activation of the motional degrees of freedom of the organic ligands, which in turn modifies the excitonic states localized in the inorganic plane. The good match of the vast majority of the DFT calculated Raman peaks with experimental ones gives us confidence in claiming that the theoretically unobserved strong low energy peaks must fall outside the simple harmonic, non-resonant framework used to calculate the Raman intensities. In other words, this experimental-theoretical comparison further suggests an incipient role of lattice anharmonicity in the behavior of the low-energy optical phonons. Finally, polarized Raman spectroscopy on single crystals demonstrated a strong anisotropy of the 12 meV phonon along the [100] crystal direction, resembling the previously observed emission anisotropy of the X_2 exciton, and therefore suggesting an important coupling between the two entities. Similar anisotropic Raman scattering was also recently found in 2D MHPs.[59]

We conclude by remarking that MOCs like the $[AgSePh]_\infty$ provide the expansion of the hybrid quantum wells materials class beyond the perovskites-like lattice of the 2D MHPs. HQWs are an ideal test bed for condensed-matter theories developing a detailed description of many body phenomena impacting the vast class of quantum materials. This includes and does not limit to coherent phonon generation, polaronic effects, Jahn–Teller-type distortion, or spin-orbit coupling.[2] Crucial advantages brought by HQWs in the experimental studies feature the facile manipulation and substitution of chemical constituents impacting the dimensionality, polarity, and rigidity of the supramolecular architecture.[60,61] All these free parameters can be used to tune the charge carriers' confinement, their dielectric screening, and their interaction with the lattice.[62] This tunability finally provides an exceptional chance for optimizing the performances of HQWs to be used in optoelectronic devices, from light emission devices to photodetectors and solar cells.

4. Experimental Section

Synthesis of $[AgSePh]_\infty$ (Silver Benzeneselenolate): The films were synthesized according to a protocol previously described in ref. [6]. Briefly, 10 nm thin films of silver were thermally evaporated on fused silica substrates. Subsequently, the Ag films were exposed to UV ozone for 10 min to oxidize silver. The oxidized silver films were reacted with benzeneselenol (PhSeH) by vapor transport for 2 h in an oven at 80 °C. The samples were rinsed in IPA to remove the unreacted benzeneselenol and N_2 dried.

Steady-state Absorption Spectroscopy: Temperature-dependent absorption spectra were obtained by measuring transmission spectra on a commercial PerkinElmer Lambda 1050 UV/Vis/NIR spectrometer. The samples were mounted in a nitrogen flow cryostat (Linkam THMS350V).

Photoluminescence and steady-state Raman Spectroscopy: Low-temperature photoluminescence and Raman signal were collected by a confocal microscope (inVia Raman Microscope Renishaw) using a 20X objective and an excitation wavelength of 442 nm and 532 nm, respectively. The samples were mounted in a nitrogen flow cryostat (Linkam THMS350V). For polarization-resolved Raman measurements, a fixed linear polarizer aligned with the grating and a rotatable lambda-half wave plate were inserted into the detection path. This allowed us to detect both co- and cross-polarized photons with the same polarization incident on the grating.

Transient Absorption Spectroscopy: We used an ultrafast transient absorption system with a tunable pump and white-light probe to measure the differential transmission through thin benzene silverselenolate films supported on quartz substrates. The laser system consists of a regeneratively amplified Ti:sapphire oscillator (Coherent Libra), which delivers 4 mJ pulse energies centered at 800 nm with a 1 kHz repetition rate. The pulse duration of the amplified pulse is ≈80 fs. The laser output was split by an optical wedge to produce the pump and probe beams and the pump beam wavelength was tuned by an optical parametric amplifier (Coherent OPerA). The pump beam was focused onto the sample by a spherical lens at near-normal incidence (spot size FWHM ≈300 μm). The probe beam was focused onto a sapphire plate to generate a white-light continuum probe, which was collected and refocused onto the sample by a spherical mirror (spot size FWHM ≈150 μm). The transmitted white light was collected and analyzed with a commercial absorption spectrometer (Helios, Ultrafast Systems LLC). Pulse-to-pulse fluctuations of the white light continuum were accounted for by a simultaneous reference

measurement of the continuum. Pump and probe beams were linearly cross-polarized and any scattered pump-light into the detection path was filtered by a linear polarizer. The time delay was adjusted by delaying the pump pulse with a linear translation stage (minimum step size 16 fs). The sample was mounted directly on the cold finger of a He-flow cryostat (Janis ST-500) by silver paste. The temperature was measured at a cold finger. All measurements were conducted in vacuum ($p \approx 10^{-5}$ mbar).

DFT Calculations for the Raman Modes: Density functional theory (DFT) and density functional perturbation theory (DFPT) simulations are performed using the QuantumESPRESSO package,[63–65] which adopts plane waves and pseudopotentials for the description of the valence electron density. In all simulations, the Perdew, Burke, and Ernzerhof (PBE) exchange and correlation function is adopted. The electronic band structure and the phonon dispersion are calculated for the herringbone-like structure.[5] In order to approximately estimate the Raman intensities, norm-conserving pseudopotentials were chosen. The pseudopotentials were taken from the ONCV dataset,[66,67] and a wavefunction cutoff of 80 Ry allowed the convergence of the total energy to better than 10 meV per atom. A Monkhorst-Pack grid of $4 \times 4 \times 1$ shifted from the Γ point is used for integration in the reciprocal space. In order to obtain the lattice vibrational modes both the lattice structure and the atomic positions were optimized until the total energy difference among subsequent steps was $<5.2 \times 10^{-4}$ Ry and the forces on atoms $<1 \times 10^{-6}$ Ry per a.u.. Phonon dispersions were obtained with DFPT and with finite displacements using the Phonopy package.[68] The approximated (see SI for details) Raman intensities have been obtained with the approach proposed by Lazzeri and Mauri.[69] The results are approximate since the third-order derivative of the correction terms introduced by PBE over LDA exchange and correlation potential with respect to the charge density are missing, but the small additional contribution is irrelevant to the scope of the present analysis. Input and output files for the results reported in the manuscript are available at Materials Cloud Archive 2023.6 (2023).[70]

Supporting Information

Supporting Information is available from the Wiley Online Library or from the author.

Acknowledgements

Work at the Molecular Foundry was supported by the Center for Novel Pathways to Quantum Coherence in Materials, Office of Science, Office of Basic Energy Sciences, of the U.S. Department of Energy under contract no. DE-AC02-05CH11231. Work at TUM was supported by the Deutsche Forschungsgemeinschaft (DFG) through SPP-2244 "2D Materials – Physics of van der Waals [hetero]structures" via Grant KA 5418/1-1. P.B. acknowledges funding from the SUPER (supercomputing unified platform—Emilia-Romagna) regional project. The United Kingdom STFC Scientific Computing Department and the Italian CINECA consortium are acknowledged for providing the high-performance computing resources through the ISCRA-C grant HP10CZHPHI and the SCARF cluster.

Open Access Funding provided by Universita degli Studi di Bologna within the CRUI-CARE Agreement.

Conflict of Interest

The authors declare no conflict of interest.

Author Contributions

C.K. and L.M. conceived, designed the experiments, and analyzed the experimental data. P.B. run the DFT calculations. L.M. synthesized the material. C.K. and L.M. performed transient absorption spectroscopy at the Molecular Foundry. L.M. performed Raman spectroscopy at CNST. The manuscript was written with inputs from all the authors.

Data Availability Statement

The data that support the findings of this study are available from the corresponding author upon reasonable request.

Keywords

anharmonic lattice vibrations, exciton-phonon coupling, Fröhlich interaction, hybrid quantum wells, metal-organic chalcogenides, Raman spectroscopy, transient absorption

Received: September 20, 2022
Revised: January 3, 2023
Published online:

[1] Y. Chen, Y. Sun, J. Peng, J. Tang, K. Zheng, Z. Liang, *Adv. Mater.* **2018**, *30*, 1703487.
[2] J.-C. Blancon, J. Even, C. C. Stoumpos, M. G. Kanatzidis, A. D. Mohite, *Nat. Nanotechnol.* **2020**, *15*, 969.
[3] B. Trang, M. Yeung, D. C. Popple, E. A. Schriber, M. A. Brady, T. R. Kuykendall, J. N. Hohman, *J. Am. Chem. Soc.* **2018**, *140*, 13892.
[4] L. Maserati, S. Pecorario, M. Prato, M. Caironi, *J. Phys. Chem. C* **2020**, *124*, 22845.
[5] W. Paritmongkol, T. Sakurada, W. S. Lee, R. Wan, P. Müller, W. A. Tisdale, *J. Am. Chem. Soc.* **2021**, *143*, 20256.
[6] L. Maserati, S. Refaely-Abramson, C. Kastl, C. T. Chen, N. J. Borys, C. N. Eisler, M. S. Collins, T. E. Smidt, E. S. Barnard, M. Strasbourg, E. A. Schriber, B. Shevitski, K. Yao, J. N. Hohman, P. J. Schuck, S. Aloni, J. B. Neaton, A. M. Schwartzberg, *Mater. Horiz.* **2021**, *8*, 197.
[7] C. Kastl, A. M. Schwartzberg, L. Maserati, *ACS Nano* **2022**, *16*, 3715.
[8] K. Yao, M. S. Collins, K. M. Nell, E. S. Barnard, N. J. Borys, T. Kuykendall, J. N. Hohman, P. J. Schuck, *ACS Nano* **2021**, *15*, 4085.
[9] W. Paritmongkol, W. S. Lee, W. Shcherbakov-Wu, S. K. Ha, T. Sakurada, S. J. Oh, W. A. Tisdale, *ACS Nano* **2022**, *16*, 2054.
[10] W. S. Lee, Y. Cho, E. R. Powers, W. Paritmongkol, T. Sakurada, H. J. Kulik, W. A. Tisdale, *ACS Nano* **2022**, *16*, 20318.
[11] K. M. McCall, C. C. Stoumpos, S. S. Kostina, M. G. Kanatzidis, B. W. Wessels, *Chem. Mater.* **2017**, *29*, 4129.
[12] Z. Guo, X. Wu, T. Zhu, X. Zhu, L. Huang, *ACS Nano* **2016**, *10*, 9992.
[13] J. Yin, H. Li, D. Cortecchia, C. Soci, J.-L. Brédas, *ACS Energy Lett.* **2017**, *2*, 417.
[14] F. Thouin, D. A. Valverde-Chávez, C. Quarti, D. Cortecchia, I. Bargigia, D. Beljonne, A. Petrozza, C. Silva, A. R. S. Kandada, *Nat. Mater.* **2019**, *18*, 349.
[15] J. M. Urban, G. Chehade, M. Dyksik, M. Menahem, A. Surrente, G. Trippé-Allard, D. K. Maude, D. Garrot, O. Yaffe, E. Deleporte, P. Plochocka, M. Baranowski, *J. Phys. Chem. Lett.* **2020**, *11*, 5830.
[16] R. A. DeCrescent, X. Du, R. M. Kennard, N. R. Venkatesan, C. J. Dahlman, M. L. Chabinyc, J. A. Schuller, *ACS Nano* **2020**, *14*, 8958.
[17] R. A. DeCrescent, N. R. Venkatesan, C. J. Dahlman, R. M. Kennard, X. Zhang, W. Li, X. Du, M. L. Chabinyc, R. Zia, J. A. Schuller, *Sci. Adv.* **2020**, *6*, eaay4900.
[18] A. Laubereau, W. Kaiser, *Rev. Mod. Phys.* **1978**, *50*, 607.
[19] L. Dhar, J. A. Rogers, K. A. Nelson, *Chem. Rev.* **1994**, *94*, 157.
[20] K. Huang, A. Rhys, N. F. Mott, *Proc. R. Soc. A* **1950**, *204*, 406.

[21] L. Zhou, J. Huang, L. Windgaetter, C. S. Ong, X. Zhao, C. Zhang, M. Tang, Z. Li, C. Qiu, S. Latini, Y. Lu, D. Wu, H. Gou, A. T. S. Wee, H. Hosono, S. G. Louie, P. Tang, A. Rubio, H. Yuan, *Nat. Mater.* **2022**, *21*, 773.
[22] S. De Silvestri, J. G. Fujimoto, E. P. Ippen, E. B. Gamble, L. R. Williams, K. A. Nelson, *Chem. Phys. Lett.* **1985**, *116*, 146.
[23] Y. Yan, E. B. Gamble, K. A. Nelson, *J. Chem. Phys.* **1985**, *83*, 5391.
[24] E. O. Göbel, K. Leo, T. C. Damen, J. Shah, S. Schmitt-Rink, W. Schäfer, J. F. Müller, K. Köhler, *Phys. Rev. Lett.* **1990**, *64*, 1801.
[25] S. Sim, D. Lee, A. V. Trifonov, T. Kim, S. Cha, J. H. Sung, S. Cho, W. Shim, M.-H. Jo, H. Choi, *Nat. Commun.* **2018**, *9*, 351.
[26] T. E. Stevens, J. Kuhl, R. Merlin, *Phys. Rev. B* **2002**, *65*, 144304.
[27] J. Fu, M. Li, A. Solanki, Q. Xu, Y. Lekina, S. Ramesh, Z. X. Shen, T. C. Sum, *Adv. Mater.* **2021**, *33*, 2006233.
[28] Y. Guo, O. Yaffe, T. D. Hull, J. S. Owen, D. R. Reichman, L. E. Brus, *Nat. Commun.* **2019**, *10*, 1175.
[29] I. P. Ipatova, A. A. Maradudin, R. F. Wallis, *Phys. Rev.* **1967**, *155*, 882.
[30] P. G. Klemens, *Phys. Rev.* **1966**, *148*, 845.
[31] G. Scamarcio, V. Spagnolo, G. Ventruti, M. Lugará, G. C. Righini, *Phys. Rev. B* **1996**, *53*, R10489.
[32] B. Miller, J. Lindlau, M. Bommert, A. Neumann, H. Yamaguchi, A. Holleitner, A. Högele, U. Wurstbauer, *Nat. Commun.* **2019**, *10*, 807.
[33] H. Fröhlich, *Adv. Phys.* **1954**, *3*, 325.
[34] K. Miyata, D. Meggiolaro, M. T. Trinh, P. P. Joshi, E. Mosconi, S. C. Jones, F. De Angelis, X.-Y. Zhu, *Sci. Adv.* **2017**, *3*, e1701217.
[35] J. A. Steele, P. Puech, M. Keshavarz, R. Yang, S. Banerjee, E. Debroye, C. W. Kim, H. Yuan, N. H. Heo, J. Vanacken, A. Walsh, J. Hofkens, M. B. J. Roeffaers, *ACS Nano* **2018**, *12*, 8081.
[36] W. Bo, N. Weihua, X. Qiang, M. Manukumara, F. Minjun, Y. Senyun, F. Jianhui, L. Stener, Y. Tingting, W. Feng, G. T. Wee, H. P. Cholakkal, T. Y. K. Eugene, S. Z. Xiang, H. Fuqiang, S. Ranjan, Z. Guofu, G. Feng, S. T. Chien, *Sci. Adv.* **2021**, *7*, eabd3160.
[37] A. R. Srimath Kandada, C. Silva, *J. Phys. Chem. Lett.* **2020**, *11*, 3173.
[38] C. Franchini, M. Reticcioli, M. Setvin, U. Diebold, *Nat. Rev. Mater.* **2021**, *6*, 560.
[39] J. T. Devreese, *arXiv:1012.4576* [cond-mat.other], **2010**, https://doi.org/10.48550/ARXIV.1012.4576.
[40] K. P. O'Donnell, X. Chen, *Appl. Phys. Lett.* **1991**, *58*, 2924.
[41] H. Murotani, K. Ikeda, T. Tsurumaru, R. Fujiwara, S. Kurai, H. Miyake, K. Hiramatsu, Y. Yamada, *Phys. Status Solidi B* **2018**, *255*, 1700374.
[42] C. Sasaki, H. Naito, M. Iwata, H. Kudo, Y. Yamada, T. Taguchi, T. Jyouichi, H. Okagawa, K. Tadatomo, H. Tanaka, *J. Appl. Phys.* **2003**, *93*, 1642.
[43] T. J. Liptay, L. F. Marshall, P. S. Rao, R. J. Ram, M. G. Bawendi, *Phys. Rev. B* **2007**, *76*, 155314.
[44] J. Lee, E. S. Koteles, M. O. Vassell, *Phys. Rev. B* **1986**, *33*, 5512.
[45] S. Rudin, T. L. Reinecke, B. Segall, *Phys. Rev. B* **1990**, *42*, 11218.
[46] A. D. Wright, C. Verdi, R. L. Milot, G. E. Eperon, M. A. Pérez-Osorio, H. J. Snaith, F. Giustino, M. B. Johnston, L. M. Herz, *Nat. Commun.* **2016**, *7*, 11755.
[47] J. Ramade, L. M. Andriambariarijaona, V. Steinmetz, N. Goubet, L. Legrand, T. Barisien, F. Bernardot, C. Testelin, E. Lhuillier, A. Bramati, M. Chamarro, *Appl. Phys. Lett.* **2018**, *112*, 072104.
[48] V. K. Malinovsky, A. P. Sokolov, *Solid State Commun.* **1986**, *57*, 757.
[49] G. P. Johari, *J. Non-Cryst. Solids* **2002**, *307*, 114.
[50] S. C. SIRKAR, *Nature* **1935**, *136*, 759.
[51] G. Neumann, H. Vogt, *Phys. Status Solidi B* **1978**, *85*, 179.
[52] O. Yaffe, Y. Guo, L. Z. Tan, D. A. Egger, T. Hull, C. C. Stoumpos, F. Zheng, T. F. Heinz, L. Kronik, M. G. Kanatzidis, J. S. Owen, A. M. Rappe, M. A. Pimenta, L. E. Brus, *Phys. Rev. Lett.* **2017**, *118*, 136001.
[53] A. M. Sanni, S. N. Lavan, A. S. Rury, *J. Phys. Chem. C* **2020**, *124*, 13942.
[54] N. S. Dahod, A. France-Lanord, W. Paritmongkol, J. C. Grossman, W. A. Tisdale, *J. Chem. Phys.* **2020**, *153*, 044710.
[55] R. A. Cowley, *J. Phys. France* **1965**, *26*, 659.
[56] H. L. Cuthbert, A. I. Wallbank, N. J. Taylor, J. F. Corrigan, *Z. Anorg. Allg. Chem.* **2002**, *628*, 2483.
[57] W. Tao, Y. Zhang, H. Zhu, *Acc. Chem. Res.* **2022**, *55*, 345.
[58] J.-C. Blancon, A. V. Stier, H. Tsai, W. Nie, C. C. Stoumpos, B. Traoré, L. Pedesseau, M. Kepenekian, F. Katsutani, G. T. Noe, J. Kono, S. Tretiak, S. A. Crooker, C. Katan, M. G. Kanatzidis, J. J. Crochet, J. Even, A. D. Mohite, *Nat. Commun.* **2018**, *9*, 2254.
[59] B. Dhanabalan, Y.-C. Leng, G. Biffi, M.-L. Lin, P.-H. Tan, I. Infante, L. Manna, M. P. Arciniegas, R. Krahne, *ACS Nano* **2020**, *14*, 4689.
[60] A. Eichhöfer, J.-J. Jiang, H. Sommer, F. Weigend, O. Fuhr, D. Fenske, C.-Y. Su, G. Buth, *Eur. J. Inorg. Chem.* **2010**, *2010*, 410.
[61] O. Veselska, A. Demessence, *Coord. Chem. Rev.* **2018**, *355*, 240.
[62] Y. Li, X. Jiang, Z. Fu, Q. Huang, G.-E. Wang, W.-H. Deng, C. Wang, Z. Li, W. Yin, B. Chen, G. Xu, *Nat. Commun.* **2020**, *11*, 261.
[63] P. Giannozzi, S. Baroni, N. Bonini, M. Calandra, R. Car, C. Cavazzoni, D. Ceresoli, G. L. Chiarotti, M. Cococcioni, I. Dabo, *J. Phys.: Condens. Matter.* **2009**, *21*, 395502.
[64] P. Giannozzi, O. Andreussi, T. Brumme, O. Bunau, M. B. Nardelli, M. Calandra, R. Car, C. Cavazzoni, D. Ceresoli, M. Cococcioni, N. Colonna, I. Carnimeo, A. Dal Corso, S. de Gironcoli, P. Delugas, R. A. DiStasio, A. Ferretti, A. Floris, G. Fratesi, G. Fugallo, R. Gebauer, U. Gerstmann, F. Giustino, T. Gorni, J. Jia, M. Kawamura, H.-Y. Ko, A. Kokalj, E. Küçükbenli, M. Lazzeri, et al., *J. Phys.: Condens. Matter* **2017**, *29*, 465901.
[65] P. Giannozzi, O. Baseggio, P. Bonfà, D. Brunato, R. Car, I. Carnimeo, C. Cavazzoni, S. de Gironcoli, P. Delugas, F. F. Ruffino, A. Ferretti, N. Marzari, I. Timrov, A. Urru, S. Baroni, *J. Chem. Phys.* **2020**, *152*, 154105.
[66] D. R. Hamann, *Phys. Rev. B* **2013**, *88*, 085117.
[67] M. Schlipf, F. Gygi, *Comput. Phys. Commun.* **2015**, *196*, 36.
[68] A. Togo, I. Tanaka, *Scr. Mater.* **2015**, *108*, 1.
[69] M. Lazzeri, F. Mauri, *Phys. Rev. Lett.* **2003**, *90*, 036401.
[70] C. Kastl, P. Bonfà, L. Maserati, *Mater. Cloud Arch.* **2023**, *6*, 2023.